CrossMark

Crystal structure, chemical stability and electrical properties of $Sr_2MnNbO_{6-\delta}$, $Sr_2Cr_{0.5}Mn_{0.5}NbO_{6-\delta}$ and $Sr_2CuNbO_{6-\delta}$ perovskites

N. Tarasova[1] · Ph. Colomban[2] · I. Animitsa[1]

Abstract The $3d$-cation-substituted perovskites $Sr_2MnNbO_{6-\delta}$, $Sr_2Cr_{0.5}Mn_{0.5}NbO_{6-\delta}$ and $Sr_2CuNbO_{6-\delta}$ were synthesized using the solid state technique. Conductivity measurements showed that the investigated phases exhibited mixed-electronic-ionic conductivity, and the total conductivity decreased in the row $Sr_2MnNbO_{6-\delta}$–$Sr_2Cr_{0.5}Mn_{0.5}NbO_{6-\delta}$–$Sr_2CuNbO_{6-\delta}$. The O^{2-}-conductivity was measured by oxygen permeation technique, and it was found that the Cu- and Cr-containing samples exhibited ~0.5 order of magnitude higher ionic conductivities at 500 °C, and lower activation energies, 0.85 ± 0.02 and 0.90 ± 0.02 eV, respectively, than Mn-containing compound $Sr_2MnNbO_{6-\delta}$ (1.16 ± 0.03 eV). The conductivity, thermogravimetry and Raman measurements showed that these compositions did not intercalate the water and did not exhibit proton conductivity, but showed good chemical stability at high water vapour pressure. In contrast, the solid solution $Sr_{2.9-x}Cu_xNb_{1.1}O_{5.65}$ ($x = 0.07$; 0.15) with double perovskite structure was able to water uptake and to proton transport, but had a low chemical stability.

✉ N. Tarasova
  Natalia.Tarasova@urfu.ru

1 Institute of Natural Sciences and Mathematics, Ural Federal University, Yekaterinburg, Russia

2 Sorbonne Universités, UPMC Univ Paris 06, UMR 8233 CNRS, MONARIS, 75005 Paris, France

Introduction

Perovskite oxides ABO_3 have received widespread attention due to their unique properties. It is common knowledge that 90% of the elements of the periodic table are stable in a perovskite structure and that multicomponent perovskites could be synthesized by partial substitution of cations at either A- or B-sites [1]. This makes it possible to synthesize new perovskite compounds with the aim to enhance desired properties and develop new applications.

Some of the most important applications of perovskites are their using as components of solid oxide fuel cells (SOFC) and more promisingly of intermediate temperature solid oxide fuel cells (IT-SOFC) and electrolysers (IT-SOE) [2]. Perovskite oxides, as electrode material for IT-SOFC, should possess sufficiently high electronic and oxide-ion conductivities, open porosity, thermal and chemical compatibilities with the electrolyte and long-term stability in operating conditions [3, 4]. Because of these unique properties, perovskite systems may be used both as cathodes and anodes. In recent years, systems with the double perovskite structure have been investigated intensively as anode materials (especially molybdenum-containing double perovskites) and promising results have been obtained [5–7].

It should also be mentioned that perovskite materials can be employed in all-perovskite SOFCs which exhibit good characteristics [8, 9]. The all-perovskite SOFC's could increase the electrochemical and thermomechanical compatibilities of SOFC system and eliminate the interactions between electrolyte and electrode.

One of the strategies to obtain mixed conductors as potential electrode material for IT-SOFC is the introduction of transition elements with variable oxidation states (usually $3d$-elements in the periodic table) in B-sublattice of known crystalline matrix. The double perovskites, with large oxygen

deficiency, niobates and tantalates of alkaline earth elements, are the most widely studied as oxygen-ion and proton conductors. The examples are $Sr_3NbO_{5.5}$ [10, 11], $Sr_3TaO_{5.5}$ [12–14], $Ba_2CaNbO_{5.5}$ [5, 15, 16] and $Ba_2CaTaO_{5.5}$ [17]. It can be assumed that the introduction of 3d-elements in B-sublattice of double perovskites $A_2BB'O_{6-\delta}$ may lead to an increase in electronic conductivity while the high oxygen-ion conductivity is maintained. We believe that these perovskites are a good model system for the study of interrelations between the nature of 3d-elements and various high-temperature properties. At the same time, from a fundamental point of view, materials with mixed conductivity are of interest to researchers not only due to the wide variety of their practical applications in various electrochemical devices, but also as objects with interesting transport properties where the two kinds of species are mobile.

Therefore, in this paper, we focused on substituted strontium niobate in which the selected 3d-elements are Mn, Cu and Cr. The $Sr_2MnNbO_{6-\delta}$, $Sr_2CuNbO_{6-\delta}$ and $Sr_2Cr_{0.5}Mn_{0.5}NbO_{6-\delta}$ perovskites were the objects of the study. We report on the various high-temperature properties important for electrode materials. The compounds $Sr_2MnNbO_{6-\delta}$ and $Sr_2CuNbO_{6-\delta}$ were earlier described as magnetic materials [18, 19], but composition $Sr_2Cr_{0.5}Mn_{0.5}NbO_{6-\delta}$ was first synthesized and described in the present work. Moreover, we attempted to compare the properties of these phases with the Cu-substituted strontium niobates from the homogeneity range of $Sr_{2.9-x}Cu_xNb_{1.1}O_{6-\delta}$ ($x = 0.07$; 0.15), described in [20–22]. The difference between these compounds is due to the presence of strontium in the octahedral sites in the compositions $Sr_2^{cub}(Sr_{0.83}Cu_{0.07}Nb_{1.10})^{oct}O_{6-\delta}$ ($x = 0.07$) and $Sr_2^{cub}(Sr_{0.75}Cu_{0.15}Nb_{1.10})^{oct}O_{6-\delta}$ ($x = 0.15$), as opposed to the $Sr_2(MnNb)^{oct}O_{6-\delta}$, $Sr_2(CuNb)^{oct}O_{6-\delta}$ and $Sr_2(Cr_{0.5}Mn_{0.5}Nb)^{oct}O_{6-\delta}$ perovskites, where a half of B-cation sites are occupied by 3d-metal cations. As it will be shown below, this difference causes the appearance of proton transport in $Sr_{2.9-x}Cu_xNb_{1.1}O_{6-\delta}$.

In this study, we report on the synthesis, the crystal structure and characterization of $Sr_2MnNbO_{6-\delta}$, $Sr_2CuNbO_{6-\delta}$ and $Sr_2Cr_{0.5}Mn_{0.5}NbO_{6-\delta}$ perovskites as potential electrode materials. The measurements of electrical conductivity (ionic and electronic) were discussed. The chemical/structural stability of niobate ceramics to high water vapour pressure (40 bar, 550 °C, 10 h) was compared.

Experimental

Synthesis

The compositions of $Sr_2MnNbO_{6-\delta}$, $Sr_2Cr_{0.5}Mn_{0.5}NbO_{6-\delta}$, $Sr_2CuNbO_{6-\delta}$ and solid solutions $Sr_{2.9-x}Cu_xNb_{1.1}O_{6-\delta}$ ($x = 0.07$; 0.15) were prepared by a solid-state method. The high-purity powders of $SrCO_3$ (99.99% purity, VEKTON, Ukraine), Nb_2O_5 (99.99% purity, REACHIM, Russia),

Mn_2O_3 (99.99% purity, REACHIM, Russia), CuO (99.99% purity, REACIM, Russia) and Cr_2O_3 (99.99% purity, REACHIM, Russia) were used. The starting reagents were preliminary dried prior weighting; stoichiometric quantities of the reagents were mixed with ethanol in agate mortar and then heated in several steps: 800 °C—10 h, 1000 °C—10 h, 1200 °C—20 h and 1500 °C—10 h. The intermediate grindings were made after each stage.

X-ray diffraction

The X-ray powder diffraction (XRD) analyses of the ground pellets were made on a Bruker Advance D8 diffractometer with Cu K_α radiation at voltage 40 kV on a tube and a current of 40 mA. The shooting was made in the interval $2\theta = 25–75°$ at steps of 0.05θ and 1 s exposure per point. The unit-cell parameters of dried and hydrated samples were determined through Rietveld refinement using Fullprof software. The number of refined parameters were varied from 11 to 17, including a fifth-order polynomial for describing the background, unit-cell parameters, atomic coordinates. Values of the reliability factor χ^2 ranged from 1 to 2.5.

Conductivity measurements

Measuring the total conductivity

The ceramic bar samples ($30 \times 4 \times 4$ mm) used for the electrical measurements were sintered at 1550 °C for 6 h. The samples typically had a relative density of around ~95% (density of the sintered samples was determined by Archimede method). The four-probe DC measurements were performed as a function of temperature under dry and wet air (see details below). The two outer probes were used to apply current to the sample and the two inner probes to measure the resulting potential drop across the specimen. The electrodes were made from platinum wires.

The measurements of the temperature dependencies of conductivities were performed in 'dry' and 'wet' air from 1000 to 200 °C every 10–20 °C with a cooling rate of 1°/min and with 1 h equilibration times before each measurement. The 'wet' air was obtained by bubbling the air at room temperature first through distilled water and then through saturated solution of KBr ($pH_2O = 2\cdot10^{-2}$ bar). The 'dry' air was produced by flowing the gas through P_2O_5 ($pH_2O = 3.5\cdot10^{-5}$ bar). The humidity of the gases was measured by H_2O-sensor ('Honeywell' HIH-3610).

Determining the O^{2-} conductivity by permeation measurements

The method is based on the direct determination of the steady flow of oxygen through the specimen (at constant

temperature) under a small gradient of the oxygen chemical potential within the sample. The details on the oxygen permeability measurements were published earlier [23–26]. According to Wagner theory, when a dense ceramic sample having mixed oxygen ionic and electronic conductivity is placed under an oxygen chemical potential difference, the fluxes of oxygen ions and electron charge carriers in the ceramics bulk will be induced, and the oxygen permeation flux density is given by:

$$j_{O_2} = \frac{RT}{16F^2 L} \int_{P_{O_2}'}^{P_{O_2}''} \frac{\sigma_{ion}\sigma_{el}}{\sigma_{ion} + \sigma_{el}} d\ln P_{O_2}$$

where $j(O_2)$ is the O_2 flux, pO_2 is the oxygen partial pressure, R and F are the gas and Faraday's constants, T is temperature, L is the thickness of the membrane, σ_{ion} and σ_{el} are the partial ionic and electronic conductivities. When the value of ΔpO_2 is known, the conductivity factor (so-called ambipolar conductivity) $\chi_c = \frac{\sigma_{ion}\cdot\sigma_{el}}{\sigma_{ion}+\sigma_{el}}$ can be determined. This method is useful for determining small minority charge carrier conductivities. When $\sigma_{ion} << \sigma_{el}$ or $\sigma_{el} << \sigma_{ion}$, the smaller conductivity can be determined. So, in the case of mixed conductor, in which the electronic conduction predominates ($\sigma_{el} >> \sigma_{ion}$), this method allows determining the ionic conductivity σ_{ion}.

The experimental cell for oxygen permeation measurements is shown in Fig. 1. The cell includes an oxygen pump (an oxygen sensor) and the studied membrane. The measurements were performed on disks with a diameter of 12 mm and thickness of ~1.5 mm. The disks were glass-sealed into yttria-stabilized zirconia (YSZ) tube at 1000 °C. No electrodes were used on the samples for these measurements. One side of the sample disk was exposed to air. The oxygen partial pressure at the other side was reduced by using YZS oxygen pump (Fig. 1), and the value of ΔpO_2 on both sides of the pellet was monitored by YZS oxygen sensor (Fig. 1). So, the membrane was exposed under a controlled drop of oxygen chemical potential.

When the rate of the oxygen flux through the specimen became equal to the rate of removal of oxygen out of the cell, a stationary condition was established, and the value of current achieved a constant value (I). Thus, the relation between the measured electric current, that was equivalent to the oxygen flux through the specimen, the EMF (E), that corresponded to the drop of partial oxygen pressures and conductivity factor χ_c can be expressed as $\chi_c = I/E(L/S)$, where L is the thickness and S is the cross-sectional area of the specimen.

We performed some studies for the samples with a thickness of 1 cm, and there were no differences in the results obtained. So, we propose that the surface exchange process is negligible, and the oxygen flux through the membranes is limited by oxygen volume diffusion and not by the oxygen surface exchange. In this situation, $J(O_2)$ (the specific oxygen
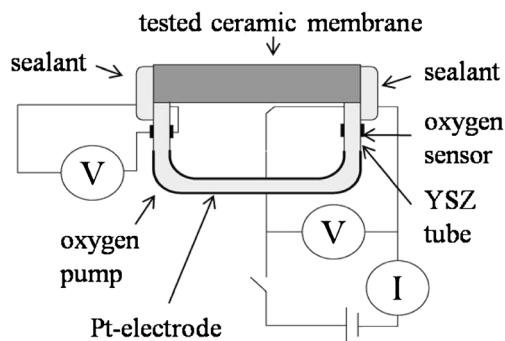

Fig. 1 Schematic drawing of the electrochemical cell used for determining the O^{2-} conductivity by permeation measurements

permeability) [25] is proportional to the ambipolar conductivity, which makes it possible to calculate the ionic conductivity.

Autoclave treatment

Autoclave treatment (protonation) was made at constant temperature and high water vapour pressure. The autoclave device 'Top Industrie' (operating range up to 600 °C and up to 90 bar H_2O) was used [27–34]. The ceramics were placed on the gold-foil holder, put in the autoclave chamber and the required volume of water was added. The water used was saturated with CO_2 at room temperature. The dwell water pressure is adjusted by controlling the maximal pressure of 40 bar when the temperature reaches ~400 °C. A small decrease of the pressure is observed during the protonation (550 °C, 10 h), which indicates consumption of water by the ceramic pellets. The pellets are then broken in two parts to make possible the Raman analysis from the pellet core to its surface.

Raman spectroscopy

A HR800 LabRam setup from Horiba Scientific Jobin Yvon, excited with 514.5 nm (Coherent Ar$^+$ ion laser) excitation (spectral range 10–4000 cm^{-1}) and a Labram Infinity from Dilor (spectral range 150–4000 cm^{-1}), excited with 532 (YAG laser) and 633 nm (He laser) were used for all Raman measurements. We used ×100 and ×50 microscope objectives (Olympus). The laser power was locked around 1 mW (at the sample). The investigations were made at room temperature in air.

Thermogravimetric analysis (TG)

TG-analysis was carried out on a STA (simultaneous thermal analyser) 409 PC analyser (Netzsch) coupled with a quadrupole mass spectrometer QMS 403 C Aëolos (Netzsch). The samples were heated at the rate of 10 °C/min in a corundum crucible under a flow of argon (99.999% purity, $pH_2O = 2.5 \times 10^{-3}$ bar) at the temperature range 40–1100 °C.

Results and discussions

XRD characterization

Room temperature X-ray diffraction (XRD) data showed that all prepared materials were single phase and characterized by a cubic symmetry with an ordinary perovskite parameter: $a = 0.3953(9)$ nm for $Sr_2MnNbO_{6-\delta}$ (Fig. 2a), $a = 0.3965(8)$ nm for $Sr_2Cr_{0.5}Mn_{0.5}NbO_{6-\delta}$ (Fig. 2c) and $a = 0.3968(1)$ nm for $Sr_2CuNbO_{6-\delta}$ (Fig. 2d). The XRD data for $Sr_2CuNbO_{6-\delta}$ are in good agreement with reference [21], but there are discrepancies in the literature on the choice of the space group for $Sr_2MnNbO_{6-\delta}$ [19, 35, 36]. Tao & Irving [35] point out that the pattern looks like a typical primitive perovskite oxide; however, the appearance of a weak peak at 2Θ 37.6° indicates some B-site ordering and, therefore, space group $Fm\overline{3}m$ was chosen for Rietveld refinement. But S.E.A. Yousif et al. have reported that $Sr_2MnNbO_{6-\delta}$ is stable in tetragonal structure [29]. M.W. Lufaso et al. [36] clarified that compound $Sr_2MnNbO_{6-\delta}$ possess shot-range cation ordering and that it is difficult to detect the extent of ordering at the local scale. Perhaps different time–temperature treatments during synthesis might lead to the different extent of ordering in B-sublattice of $Sr_2MnNbO_{6-\delta}$. The question whether this ordering is due to variations in heat treatment or to other reasons remains to be answered. Because no additional reflections were observed in the XRD pattern for the Mn-contained sample, the structural model with space group $Pm\overline{3}m$ was used for $Sr_2MnNbO_{6-\delta}$. We also attempted to adopt space group $Fm\overline{3}m$, but no improvement of the fit (R-value) was observed. So, these three compounds, including first synthesized $Sr_2Cr_{0.5}Mn_{0.5}NbO_{6-\delta}$ composition, were characterized in the same space group $Pm\overline{3}m$.

The compositions, $Sr_{2.83}Cu_{0.07}Nb_{1.1}O_{6-\delta}$ (Fig. 2e) and $Sr_{2.75}Cu_{0.15}Nb_{1.1}O_{6-\delta}$ (Fig. 2f), crystallize in the cubic space group $Fm\overline{3}m$ and show doubled perovskite parameters $a = 0.8294(3)$ nm and $a = 0.8284(1)$ nm, respectively. This is in accordance with the literature [20, 22] and indicates an ordering of B-cations. Because the B-site ordering in double perovskites $A_2BB'O_6$ depends on differences in charge between B and B′ cations and their ionic radii, the differences between Nb^{5+} and Sr^{2+} lead to long-range cation ordering in the Sr-containing phases.

Conductivity measurements

The total conductivities as a function of temperature in the dry ($pH_2O = 3.5 \times 10^{-5}$ bar) and wet ($pH_2O = 2 \times 10^{-2}$ bar) air are shown in Fig. 3. Electrical conductivity of investigated phases decreased in the row $Sr_2MnNbO_{6-\delta} - Sr_2Cr_{0.5}Mn_{0.5}NbO_{6-\delta} - Sr_2CuNbO_{6-\delta}$, and the differences between the samples were essential. The conductivity value for the most conductive sample $Sr_2MnNbO_{6-\delta}$ was 0.255 S/cm at 970°C. The activation energy for this sample was the lowest (0.34 ± 0.01 eV) compared to the other samples (~0.5 eV). The values for electrical conductivity in dry and wet atmospheres were about the same. The total conductivities for Cu-substituted strontium niobate $Sr_{2.9-x}Cu_xNb_{1.1}O_{6-\delta}$ [20] and strontium niobate $Sr_{2.91}Nb_{1.06}O_{6-\delta}$ [11] are shown for comparison. The data shown in Fig. 3 clearly indicates the influence of the nature of 3d-element on conductivities and this may be due to a change in the band gap.

The temperature dependencies of the oxygen-ion conductivities for the samples $Sr_2MnNbO_{6-\delta}$, $Sr_2Cr_{0.5}Mn_{0.5}NbO_{6-\delta}$ and $Sr_2CuNbO_{6-\delta}$ are shown in Fig. 4.

The activation energy was measured at around ~1 eV, which is typical for oxygen-ionic transport. The Cu- and Cr-containing samples exhibited higher ionic conductivities and lower activation energies (0.85 ± 0.02 and 0.90 ± 0.02 eV, respectively) than Mn-containing compound $Sr_2MnNbO_{6-\delta}$. The differences in oxygen-ion conductivities reached ~0.5 order of magnitude at 500 °C. It is obvious that the increasing oxygen deficiency may lead to the increase of oxygen ion conductivity (if the formation of defect clusters and ordering of oxygen vacancies are negligible), so, understanding of the oxidation states of the transition metals is needed to determine the oxygen deficiency. But that is beyond the scope of this study. It was shown [37] that the compound $Sr_2CuNbO_{6-\delta}$ contains high proportions of Cu^{1+} ions and oxygen vacancies, and the Cu^{2+}/Cu^{1+} ratio is 1. Therefore, a value of 0.875 was estimated for the oxygen site occupancy [37]. For the $Sr_2MnNbO_{6-\delta}$ compound, it was shown that the Mn exists in the Mn^{3+} oxidation state [35], and in ambient air, the stoichiometry was essentially $SrMn^{3+}_{0.5}Nb^{5+}_{0.5}O_3$. Unfortunately, there is no information on the oxidation state of chromium in $Sr_2Cr_{0.5}Mn_{0.5}NbO_{6-\delta}$ compound, and it is uncertain whether Cr and Mn exhibit the oxidation state of +3 in the sample obtained in air. It should also be emphasized that for correct discussion of the ionic conductivity, an analysis of the mobility of ionic carriers is also needed. Considering all these observations and the fact that mobility of oxygen depends on the nature of the B-O bond, we can conclude that it is difficult to characterize the relationship in oxygen-ion conductivities for the investigated samples. At the same time, we can assume that the compound $Sr_2CuNbO_{6-\delta}$ exhibits higher oxygen ion conductivity because of a high concentration of oxygen vacancies.

The oxygen ion transference number can be obtained from the ratio of the measured oxygen-ion conductivity and total conductivity. The values were found to be ~10^{-1} for $Sr_2CuNbO_{6-\delta}$, ~10^{-2} for $Sr_2Cr_{0.5}Mn_{0.5}NbO_{6-\delta}$ and ~10^{-4} for $Sr_2MnNbO_{6-\delta}$ at 600–700 °C (Table 1).

The variation of water vapour partial pressure does not affect significantly the conductivity, therefore, we can assume
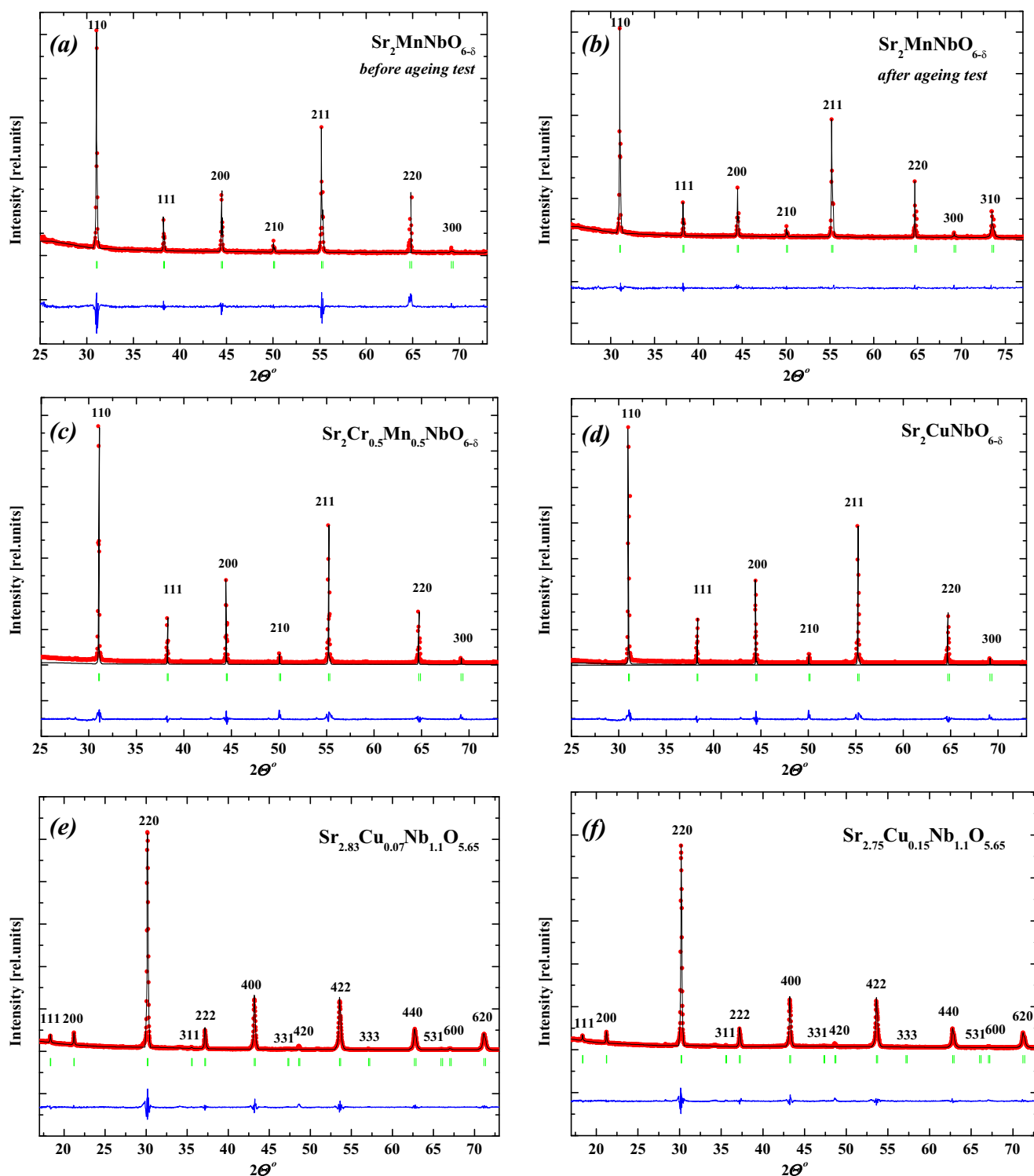
Fig. 2 Observed (*crosses*), calculated (*solid line*) and difference (*bottom*) profiles for the Rietveld refinement for $Sr_2MnNbO_{6-\delta}$ before (*a*) and after (*b*) ageing tests (550 °C, 10 h); $Sr_2Cr_{0.5}Mn_{0.5}NbO_{6-\delta}$ (*c*), $Sr_2CuNbO_{6-\delta}$ (*d*), $Sr_{2.83}Cu_{0.07}Nb_{1.1}O_{6-\delta}$ (*e*) and $Sr_{2.75}Cu_{0.15}Nb_{1.1}O_{6-\delta}$ (*f*). *Vertical bars* show the Bragg angle positions

the absence of proton conductivity in $Sr_2MnNbO_{6-\delta}$, $Sr_2Cr_{0.5}Mn_{0.5}NbO_{6-\delta}$ and $Sr_2CuNbO_{6-\delta}$. In contrast, strontium niobate $Sr_{2.91}Nb_{1.06}O_{6-\delta}$ [11] and Cu-substituted solid solution $Sr_{2.9-x}Cu_xNb_{1.1}O_{6-\delta}$ [20] show an increase in

conductivities in wet air towards to measurements in dry air below 550°C (Fig. 3). This behaviour is typical for high-temperature proton conductors and is the result of the insertion of water and the appearance of proton current carriers. These
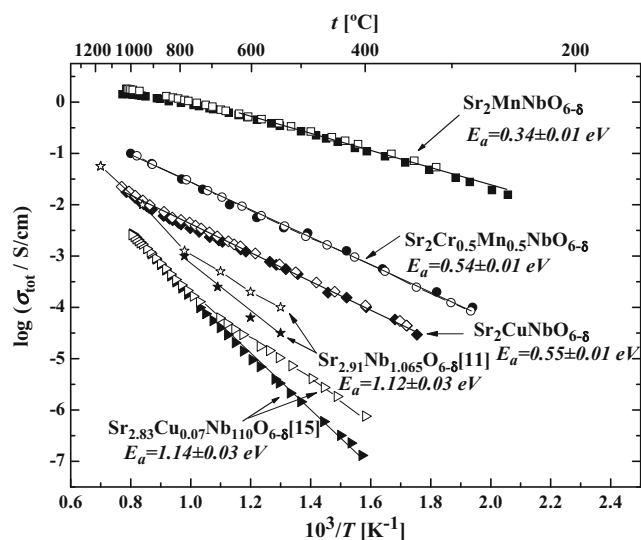
Fig. 3 The temperature dependencies of the total conductivities (*filled signs*—dry air, *open signs*—wet air). Conductivities of $Sr_{2.9-x}Cu_xNb_{1.1}O_{6-\delta}$ and $Sr_{2.91}Nb_{1.06}O_{6-\delta}$ compounds, corresponding to the literature data, are shown for comparison

Table 1 The values of the oxygen ion transference numbers, calculated as $\sigma_{ion}/\sigma_{tot}$, where σ_{tot} is total conductivity, measured independently by four-probe DC method, and σ_{ion} is the oxygen-ion conductivity, measured by permeation method

Composition	Temperature range, °C	t_{ion}
$Sr_2MnNbO_{6-\delta}$	600–700	2×10^{-4}–6×10^{-4}
$Sr_2Cr_{0.5}Mn_{0.5}NbO_{6-\delta}$	600–700	2×10^{-2}–3×10^{-2}
$Sr_2CuNbO_{6-\delta}$	600–700	1×10^{-1}–2×10^{-1}

$Sr_2MnNbO_{6-\delta}$, $Sr_2Cr_{0.5}Mn_{0.5}NbO_{6-\delta}$, $Sr_2CuNbO_{6-\delta}$ is not surprising considering that the oxygen vacancies are formed between two neighbouring 3d–cation and Nb^{5+} cation.

In summary, comparing Figs. 3 and 4, we can conclude that the nature of 3d-elements did not significantly affect the magnitude of the oxygen-ion transport, and the values for oxygen ion conductivity were close to the oxygen-ion conductivity in strontium niobate and other niobates of alkaline earth metals [11], while proton transport was negligible. At the same time, the total conductivity (Fig. 3) varied by orders of magnitude because of significant changes in electronic contribution. The presence of 3d-elements significantly increased the electron conductivity, especially for Mn-containing sample $Sr_2MnNbO_{6-\delta}$.

Structure of the samples, ageing tests and corrosion products

Because vibrational spectroscopy, especially Raman scattering, is more efficient than XRD for detecting corrosion phases, especially amorphous ones or with poor crystallinity [27, 28, 34], the Raman spectra of the samples $Sr_2MnNbO_{6-\delta}$, $Sr_2Cr_{0.5}Mn_{0.5}NbO_{6-\delta}$ and $Sr_{2.75}Cu_{0.15}Nb_{1.1}O_{6-\delta}$ were both made before (Fig. 5) and after (see further) autoclaving investigations. The observation of a spectrum indicates that some domains are locally not cubic, since no Raman bands are expected for a cubic perovskite [39–41]. Thus, the substitution in B-sublattice of strontium niobate by 3d-elements increases the distortion of perovskite structure.

For compositions with ordinary simple perovskite structure, the one mode of Nb-O stretching vibrations is observed in the Raman spectra (~810 cm⁻¹), that is consistent with the regular octahedral environment of niobium [42, 43]. Conversely, there are two modes of Nb-O stretching vibrations (~810 and ~770 cm⁻¹) for double perovskite $Sr_{5.51}Cu_{0.29}Nb_{2.2}O_{11.3}$ due to different environments of niobium as a result of the presence of oxygen vacancies.

After autoclaving investigations, the phases with complete substitution of alkaline earth element in the B-sublattice $Sr_2MnNbO_{6-\delta}$, $Sr_2Cr_{0.5}Mn_{0.5}NbO_{6-\delta}$ and $Sr_2CuNbO_{6-\delta}$ exhibit good chemical stability (Fig. 6). This is confirmed by the lack of any Raman signature in the 3200–3500 cm⁻¹ range

differences can be explained by the presence of divalent cations Sr^{2+} at B-cation sites. Differences in the sizes and charges of Sr^{2+} and Nb^{5+} ions lead to chess-type ordering between B-cations, and the oxygen vacancy is formed between Sr^{2+} and Nb^{5+} cations. It means that Sr^{2+} adopts a coordination number less than six. From a crystallo-chemical point of view, the presence of coordination-unsaturated polyhedrons in perovskite-related structures makes possible the water dissociative insertion from gas phase [17, 38]. In other words, the oxygen vacancies are filled with oxygen from the water molecule, and the coordination number comes to 6 again. The tetrahedral coordination is unstable for Sr^{2+}, therefore, the water insertion and formation of proton defects can take place. The absence of proton transport in studied compounds
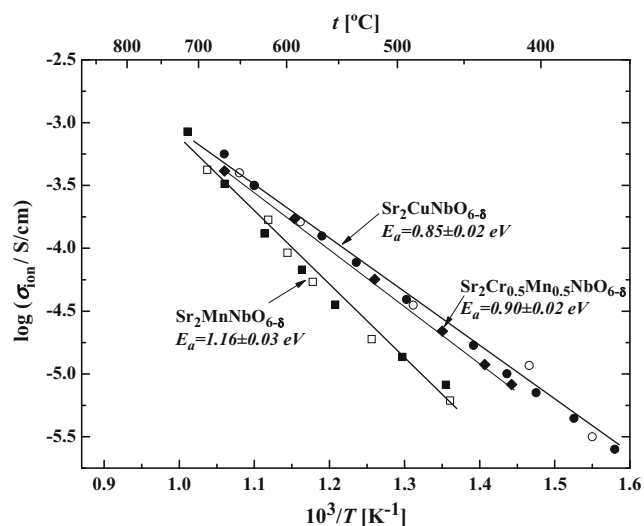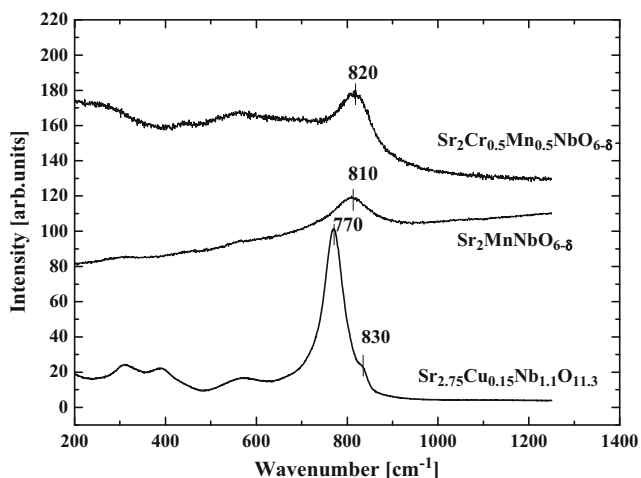

Fig. 4 The temperature dependencies of the oxygen-ion conductivities (*open signs*—wet air, *filled signs*—dry air)

Fig. 5 Raman spectra for compositions $Sr_2MnNbO_{6-\delta}$, $Sr_2Cr_{0.5}Mn_{0.5}NbO_{6-\delta}$ and $Sr_{2.75}Cu_{0.15}Nb_{1.1}O_{6-\delta}$ before ageing tests

Fig. 7 TG-data of $Sr_2MnNbO_{6-\delta}$, $Sr_2Cr_{0.5}Mn_{0.5}NbO_{6-\delta}$ and $Sr_{2.83}Cu_{0.07}Nb_{1.1}O_{6-\delta}$ after ageing tests (550 °C, 10 h)

where the signature of hydroxides should appear [37, 28]. They almost do not change in mass after autoclaving and do not intercalate the water as confirmed by TGA. Conversely Cu-substituted strontium niobates within the homogeneity range $Sr_{2.9-x}Cu_xNb_{1.1}O_{6-\delta}$ ($x = 0.07; 0.15$) react with water (Fig. 7).

XRD patterns for $Sr_2MnNbO_{6-\delta}$, $Sr_2Cr_{0.5}Mn_{0.5}NbO_{6-\delta}$ and $Sr_2CuNbO_{6-\delta}$ before and after autoclaving were the same, and additional peaks of possible impurities were not observed. The lattice parameters and crystal structure were also refined by Rietveld analysis. Fig.2b shows the result of Rietveld fit for $Sr_2MnNbO_{6-\delta}$ after 10 h of ageing tests. A good agreement between the calculated profiles and the experimental data was observed as confirmed by the reliability factors ($R_{wp} = 6.23$, $R_e = 3.82$, $\chi^2 = 1.86$).

In contrast, the compositions of $Sr_{2.83}Cu_{0.07}Nb_{1.1}O_{6-\delta}$ and $Sr_{2.75}Cu_{0.15}Nb_{1.1}O_{6-\delta}$ are capable of water uptake/loss (Fig. 7) and proton transport can occur, as it was shown earlier [20, 22].
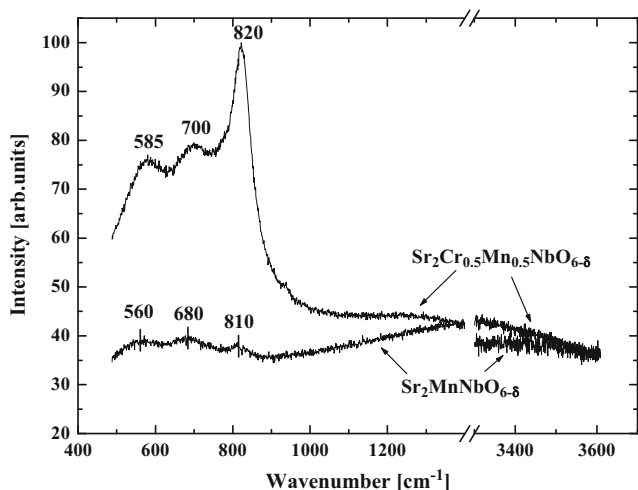
At the same time, these compositions have poor chemical stability.

Fig. 6 Raman spectra for compositions $Sr_2MnNbO_{6-\delta}$ and $Sr_2Cr_{0.5}Mn_{0.5}NbO_{6-\delta}$ after ageing tests (550 °C, 10 h)
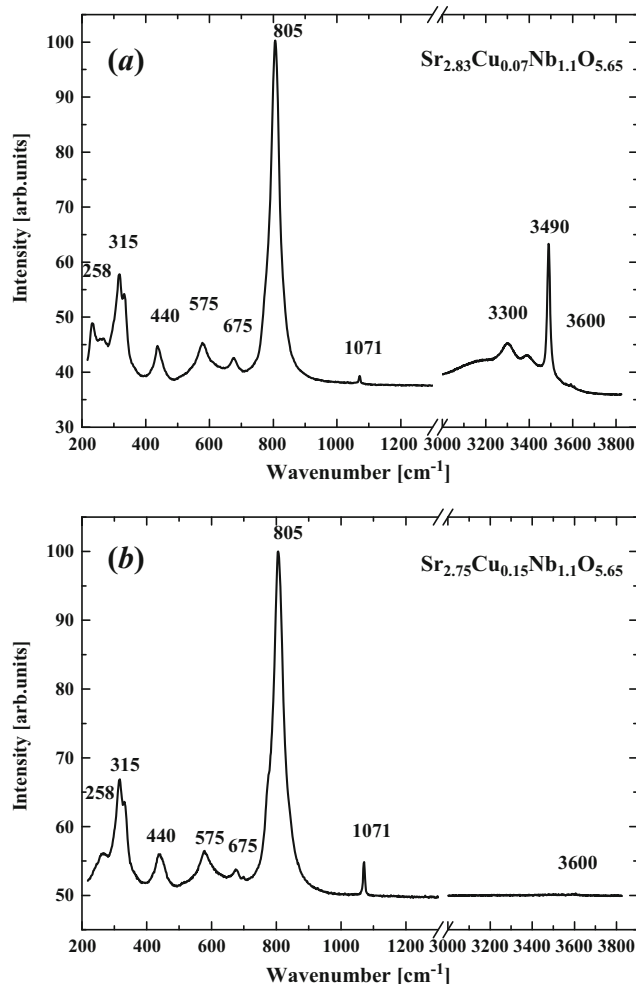
Fig. 8 Raman spectra for $Sr_{2.83}Cu_{0.07}Nb_{1.1}O_{6-\delta}$ (a) and $Sr_{2.75}Cu_{0.15}Nb_{1.1}O_{6-\delta}$ (b) after ageing tests (550 °C, 10 h)

Ageing tests results for $Sr_{2.83}Cu_{0.07}Nb_{1.1}O_{6-\delta}$ and $Sr_{2.75}Cu_{0.15}Nb_{1.1}O_{6-\delta}$ are summarized in Fig. 8a, b, respectively. The formation of $SrCO_3$ is confirmed by characteristic modes at 258 and 1071 cm^{-1} [44–46]. The modes in the region 3300–3600 cm^{-1} correspond to the stretching vibrations of oxygen-hydrogen bonds assigned to strontium hydroxides. The rather well-defined TGA loss at ~400 °C fit well with the dehydration of $Sr(OH)_2$.

Conclusions

The $3d$-cation substituted perovskites $Sr_2MnNbO_{6-\delta}$, $Sr_2Cr_{0.5}Mn_{0.5}NbO_{6-\delta}$, $Sr_2CuNbO_{6-\delta}$ and solid solution $Sr_{2.9-x}Cu_xNb_{1.1}O_{6-\delta}$ ($x = 0.07; 0.15$) were synthesized using solid state techniques. The Rietveld refinements show that the samples $Sr_2MnNbO_{6-\delta}$, $Sr_2Cr_{0.5}Mn_{0.5}NbO_{6-\delta}$ and $Sr_2CuNbO_{6-\delta}$ exhibit simple perovskite structures without noticeable ordering of the octahedral cations. In contrast, the compositions of solid solution $Sr_{2.9-x}Cu_xNb_{1.1}O_{6-\delta}$ ($x = 0.07; 0.15$) have double perovskite structure because of long range ordering of the octahedral site cations. These differences can be explained by the presence of divalent cations Sr^{2+} at B-cation sites in $Sr_{2.9-x}Cu_xNb_{1.1}O_{6-\delta}$, while in the niobates $Sr_2MnNbO_{6-\delta}$, $Sr_2Cr_{0.5}Mn_{0.5}NbO_{6-\delta}$ and $Sr_2CuNbO_{6-\delta}$ a half of B-cation sites are occupied by $3d$-metal cations.

Conductivity measurements showed that the investigated phases exhibited mixed electronic-ionic conductivity and the introduction of 3d-elements in B-sublattice significantly increased electronic conductivity, especially for Mn-containing sample $Sr_2MnNbO_{6-\delta}$. The presence of 3d-elements did not lead to significant change in oxygen-ion conductivity in comparison with electronic conductivities. At the same time, the Cu and Cr-containing samples exhibited ~0.5 order of magnitude higher ionic conductivities at 500 °C, and lower activation energies, 0.85 and 0.90 eV, respectively, than Mn-containing compound.

The TG and Raman measurements showed that the compositions with simple perovskite structure $Sr_2CuNbO_{6-\delta}$, $Sr_2Cr_{0.5}Mn_{0.5}NbO_{6-\delta}$ and $Sr_2MnNbO_{6-\delta}$ did not intercalate the water and exhibited good chemical stability at high water vapour pressure. The compositions $Sr_{2.83}Cu_{0.07}Nb_{1.1}O_{6-\delta}$ and $Sr_{2.75}Cu_{0.15}Nb_{1.1}O_{6-\delta}$, in contrast, were capable of water uptake and proton transport, but these compositions showed poor chemical stability at high water vapour pressure.

This investigation indicates that the compositions $Sr_2CuNbO_{6-\delta}$, $Sr_2Cr_{0.5}Mn_{0.5}NbO_{6-\delta}$ and $Sr_2MnNbO_{6-\delta}$ combine high transport properties and the chemical stability that allows to consider these phases as promising materials for the creation of oxygen-permeable membranes as well as electrodes for solid oxide fuel cells.

References

1. Pena MA, Fierro JLG (2001) Chemical structures and performance of perovskite oxides. Chem Rev 101:1981–2017

2. Tarancón A (2009) Strategies for Lowering Solid Oxide Fuel Cells Operating Temperature. Energies 2:1130–1150

3. Perovskite oxide for solid oxide fuel cell. Ed. T. Ishihara, Springer, 2009

4. Solid State Electrochemistry II: Electrodes, Interfaces and Ceramic Membranes. Ed. V. V. Kharton. Wiley-VCH, 2011

5. Liu Q, Bugaris DE, Xiao G, Chmara M, Ma S, Loye H-C, Amiridis MD, Chen F (2011) Sr2Fe1.5Mo0.5O6−δ as a regenerative anode for solid oxide fuel cells. J. Power Sources 196:9148–9153

6. Howell TG, Kuhnell CP, Reitz TL, Sukeshini AM, Singh RN (2013) A2MgMoO6 (A = Sr,Ba) for use as sulfur tolerant anodes. J. Power Sources 231:279–284

7. He B, Wang Z, Zhao L, Pan X, Wu X, Xia C (2013) Ti-doped molybdenum-based perovskites as anodes for solid oxide fuel cells. J. Power Sources 241:627–633

8. Li H, Tian Y, Wang Z, Qie F, Li Y (2012) An all perovskite direct methanol solid oxide fuel cell with high resistance to carbon formation at the anode. RSC Adv. 2:3857–3863

9. Sammes N, Du H Fabrication and properties of anode-supported tubular IT-SOFC based on lanthanum gallate. Advanced in Solid Oxide Fuel Cells: Ceramic Engineering and Science Proceedings. V.26. № 4. P. 33-40

10. Jalarvo N, Haavik C, Kongshaug C, Norby P, Norby T (2009) Conductivity and water uptake of Sr4(Sr2Nb2)O11·nH2O and Sr4(Sr2Ta2)O11·nH2O. Solid State Ionics 180:1151–1156

11. Glöckner R, Neiman A, Larring Y, Norby T (1999) Protons in Sr3(Sr1+xNb2-x)O9-3x/2 perovskite. Solid State Ionics 125:369–376

12. Animitsa I, Neiman A, Sharafutdinov A, Nochrin S (2000) Strontium tantalates with perovskite-related structure. Solid State Ionics 136-137:265–271

13. Animitsa I, Neiman A, Titova S, Kochetova N, Isaeva E, Sharafutdinov TN, Ph C (2003) Phase relations during water incorporation in the oxygen and proton conductor Sr6Ta2O11. Solid State Ionics 156:95–102

14. Animitsa I, Denisova T, Neiman A, Nepryahin A, Kochetova N, Zhuravlev N, Colomban P (2003) States of H+-Containing Species and Proton Migration Forms in Hydrated Niobates and Tantalates of Alkaline-Earth Metals with a Perovskite-Related Structure. Solid State Ionics 62-163:73–81

15. Animitsa I, Neiman A, Kochetova N, Korona D, Sharafutdinov A (2006) Chemical diffusion of water in the double perovskites Ba4Ca2Nb2O11 and Sr6Ta2O11. Solid State Ionics 177:2363–2368

16. Animitsa IE (2009) High-Temperature Proton Conductors with Structure-Disordered Oxygen Sublattice. Russian Journal of Electrochemistry 45(6):668–676

17. Baliteau S, Mauvy F, Fourcade S, Grenier JC (2009) Investigation on double perovskite Ba4Ca2Ta2O11. Solid State Sciences 11:1572–1575

18. Sun Z, Chen XH, Fan R, Luo XG, Li L (2003) Structure and magnetic properties of perovskite Sr2CuNbO6-δ. J. Physics and Chemistry of Solids 64:59–62

19. Yousif SEA, Yassin OA (2010) The electronic and magnetic properties of Sr2MnNbO6, Sr2FeMoO6 and Sr2NiRuO6 double

perovskites: An LSDA+U+SOC study. J. Alloys and Compounds 50:456–460

20. Animitsa I, Dogodaeva E, Zabolotskaya E (2010) Structure and Electrical Properties of Oxygen Deficient Strontium Copper Niobate. Russian Journal of Inorganic Chemistry 55(2):254–260

21. Liu Y, Withers RL, Brink F, Noren L (2004) Cubic perovskite-related phases in the ternary SrO–CuO–Nb2O5 system. J. Solid State Chemistry 177:3140–3148

22. Dogodaeva EN, Tarasova NA, Animitsa IE (2010) The study of water uptake and electrical properties of Sr5.8-xCuxNb2.2O11.3. International Scientific Journal for Alternative Energy and Ecology (Russian journal) 6:43–47

23. Riess I (1997) Electrochemistry of mixed ionic–electronic conductors. Handbook of Solid State Electrochemistry. CRC Press 1997

24. Patrakeev MV, Leonidov IA, Kozhevnikov VL, Tsidilkovskii VI, Demin AK, Nikolaev AV (1993) The oxygen permeation through YBa2Cu3O6+x. Solid State Ionics 66:61–67

25. Naumovich E, Kharton V, Marques F.M.B. (2004) Mixed Ionic Electronic Conducting Perovskites tor Advanced Energy Systems. 2004. Kluwer Academic Publishers: 185-198

26. Mauvy F, Fouletier J. (2012) Determonation of thermodynamic and Transport Properties of Non-Stoichometric Oxides, Stoichiometry and Materials Science - When Numbers Matter, ISBN: 978-953-51-1512-1

27. Slodczyk A, Zaafrani O, Sharp MD, Kilner JA, Dabrowski B, Lacroix O, Colomban P (2013) Testing the Chemical/Structural Stability of Proton Conducting Perovskite Ceramic Membranes by in Situ/ex Situ Autoclave Raman Microscopy. Membranes 3: 311–330

28. Upasen S, Batocchi P, Mauvy F, Slodczyk A, Colomban P (2015) Protonation and structural/chemical stability of Ln2NiO4+δ ceramics vs. H2O/CO2: high temperature / water pressure ageing tests. Journal of Alloys and Compounds 622:1074–1085

29. Sala B, Grasset F, Lacroix O, Sirat A, Rhamouni K, Keddam M, Takenouti H, Goeuriot D, Bendjeriou B, Colomban Ph, Slodczyk A, Pourcelly G, Van der Lee A, Sanchez JG, Patent EP 11/10/201212773302.0-1360

30. Chick LA, Marina OA, Coyle CA, Thomsen EC (2013) Effects of temperature and pressure on the performance of a solid oxide fuel cell running on steam reformate of kerosene. Journal of Power Sources 236:341–349

31. Magistri L, Traverso A, Cerutti F, Bozzolo M, Costamagna P, Massardo AF (2005) Modelling of Pressurised Hybrid Systems Based on Integrated Planar Solid Oxide Fuel Cell (IP-SOFC) Technology. Fuel Cells 5:80–96

32. Yang WJ, Park SK, Kim TS, Kim JH, Sohn JL, Ro ST (2006) Design performance analysis of pressurized solid oxide fuel cell/gas turbine hybrid systems considering temperature constraints. Journal of Power Sources 160:462–473

33. Burbank W Jr, Witmer DD, Holcomb F (2009) Model of a novel pressurized solid oxide fuel cell gas turbine hybrid engine. Journal of Power Sources 193:656–664

34. Upasen S, Batocchi P, Mauvy F, Slodczyk A, Colomban P (2015) Chemical and structural stability of La0.6Sr0.4Co0.2Fe0.8O3-d ceramic vs. medium/high water vapor pressure. Ceramics International 41:14137–14147

35. Tao S, Irvine JTS (2002) Study on the structural and electrical properties of the double perovskite oxide SrMn0.5Nb0.5O3−δ. J. Mater. Chem. 12:2356–2360

36. Lufaso MW, Woodward PM (2004) Jahn-Teller distortions, cation ordering and octahedral tilting in perovskites. Acta Cryst B60:10–20

37. Sun Z, Chen XH, Fan R, Luo XG, Li L (2003) Structure and magnetic properties of perovskite Sr2CuNbO6−δ. J. Physics and Chemistry of Solids 64:59–62

38. Animitsa I (2010) Double perovskites with structure-disordered oxygen sublattice as high-temperature proton conductors. Perovskites: Structure, Properties and Uses. P. 501-524

39. Slodczyk A, Colomban P (2010) Probing the Nanodomain Origin and Phase Transition Mechanisms in (Un)Poled PMN-PT Single Crystals and Textured Ceramics. Materials 3:5007–5029

40. Laiho R, Lisunov KG, Lähderanta E, Stamov VS, Zakhvalinskii VS, Colomban P, Petrenko PA, Stepanov YP (2005) Lattice distortions, magnetoresistance and hopping conductivity in LaMnO3+δ. J. Phys.:Condens. Matter 17:105–118

41. Leonidov IA, Patrakeev MV, Bahteeva JA, Mitberg EB, Kozhevnikov VL, Colomban P, Poeppelmeier KR (2006) High-temperature phase equilibria in the oxide systems SrFe1-xGaxO2.5 - SrFe1-xGaxO3 (x = 0, 0.1, 0.2). J. of Solid State Chemistry 179:1093–1099

42. Colomban P, Romain F, Neiman A, Animitsa I (2001) Double perovskites with oxygen structural vacancies:Raman spectra, conductivity and water uptake. Solid State Ionics 145:339–347

43. Gouadec G, Colomban P (2007) Raman Spectroscopy of nanomaterials: How spectra relate to disorder, particle size and mechanical properties. Progress in Crystal Growth and Characterization of Materials 53(1):1–56

44. RRUFF, Strontianite-SrCO3. RRUFF Project, Department of Geosciences, University of Arizona, AZ, USA

45. Kaabar W, Bott S, Devonshire R (2011) Raman spectroscopic study of mixed carbonate materials. Spectrochimica Acta Part A: Molecular and Biomolecular Spectroscopy 78:136–141

46. Cuza AI (2009) Anal Şt Univ. Iaşi Geologie. V.2. P.97